NIH Public Access
Author Manuscript
IEEE Trans Biomed Eng. Author manuscript; available in PMC 2010 July 28.

Published in final edited form as:
IEEE Trans Biomed Eng. 2010 June ; 57(6): 1273–1284. doi:10.1109/TBME.2009.2040022.

Large-Scale Propagation of Ultrasound in a 3-D Breast Model Based on High-Resolution MRI Data

Gheorghe Salahura,
Department of Electrical and Computer Engineering, University of Rochester, Rochester, NY 14627 USA

Jason C. Tillett [Member, IEEE],
Department of Electrical and Computer Engineering, University of Rochester, Rochester, NY 14627 USA

Leon A. Metlay, and
Department of Pathology and Laboratory Medicine, University of Rochester, Rochester, NY 14627 USA

Robert C. Waag [Life Fellow, IEEE]
Departments of Electrical and Computer Engineering and Imaging Sciences, University of Rochester, Rochester, NY 14627 USA

Jason C. Tillett: tillett@ece.rochester.edu; Leon A. Metlay: leon_metlay@urmc.rochester.edu; Robert C. Waag: waag@ece.rochester.edu

Abstract

A 40 × 35 × 25-mm^3 specimen of human breast consisting mostly of fat and connective tissue was imaged using a 3-T magnetic resonance scanner. The resolutions in the image plane and in the orthogonal direction were 130 μm and 150 μm, respectively. Initial processing to prepare the data for segmentation consisted of contrast inversion, interpolation, and noise reduction. Noise reduction used a multilevel bidirectional median filter to preserve edges. The volume of data was segmented into regions of fat and connective tissue by using a combination of local and global thresholding. Local thresholding was performed to preserve fine detail, while global thresholding was performed to minimize the interclass variance between voxels classified as background and voxels classified as object. After smoothing the data to avoid aliasing artifacts, the segmented data volume was visualized using iso-surfaces. The isosurfaces were enhanced using transparency, lighting, shading, reflectance, and animation. Computations of pulse propagation through the model illustrate its utility for the study of ultrasound aberration. The results show the feasibility of using the described combination of methods to demonstrate tissue morphology in a form that provides insight about the way ultrasound beams are aberrated in three dimensions by tissue.

Index Terms

Breast morphology; connective tissue segmentation; ultrasound aberration; visualization

Correspondence to: Gheorghe Salahura.

He is now with the Center for Neural Development and Disease, University of Rochester Medical Center, Rochester, NY 14627 USA (salahuragh@yahoo.com).

NIH-PA Author Manuscript
NIH-PA Author Manuscript
NIH-PA Author Manuscript

NIH-PA Author Manuscript

NIH-PA Author Manuscript

NIH-PA Author Manuscript

I. Introduction

Ultrasound is widely used for imaging in medical applications [1], [2]. Advantages of ultrasound are that it can be noninvasive, involves no ionizing radiation at diagnostic imaging intensities, is capable of real-time imaging, and uses instruments that are portable and relatively inexpensive. However, an important limitation in current ultrasound imaging is that resolution and contrast can be severely reduced by focus degradation from aberration in the propagation path between the imaging probe and the imaged region [3], [4].

To understand the way aberration is produced by tissue, an accurate acoustic model of tissue morphology is needed for calculation of ultrasound beam propagation [5]–[7]. Previous work in two dimensions utilized stained [8] cross sections of breast, abdomen, and chest wall to map visualized tissue components, i.e., fat, muscle, connective tissue, cartilage, or bone to published acoustic properties [9]–[11] of the tissues. Calculation of pulse-wave propagation through the models agreed qualitatively with observed aberration, i.e., time-shift calculations, amplitude variations, and waveform distortion, but lacked quantitative agreement because the measured propagation was 3-D. Since these calculations were performed in two dimensions, efficient methods for the calculation of pulse-wave propagation over a large number of wavelengths in three dimensions have become available [12], [13]. The combination of accurate acoustic modeling in three dimensions and newly available methods for computation of pulse-wave propagation allows quantitative comparisons of calculations and measurements.

Use of stained sections in three dimensions has been developed [14] and extended [15] to solve problems of cross-section registration, interpolation between cross sections, and variability of stain contrast from cross section to cross section. These techniques allow accurate pulse-wave propagation calculations in three dimensions but the scale of the models is limited by slide preparation techniques in which manageable cross sections are typically only on the order of a centimeter. Using large stained sections of breast is particularly challenging because some sections can contain morphology that can be damaged during slide preparation. Larger scale slices of human anatomy and corresponding images acquired with magnetic resonance imaging (MRI) and X-ray computed tomography (CT) are available from The Visible Human Project [16] and have been used for calculation of ultrasound propagation through breast [17]. However, these MRI and CT data either lack resolution for simulation of clinical-frequency pulse-wave propagation or are restricted to a single dataset that does not allow a complete statistical description of aberration caused by breast because only a single sample of an ensemble is available. Higher resolution images using MRI or CT [18] are obvious choices for further model development but MRI is preferred because CT has poor soft-tissue contrast.

The use of MRI with isotropic high resolution, e.g., between 0.1 and 0.2 mm, to show tissue morphology has scientific merit for other reasons. Resolution in clinical MRI scans is typically about 1.0 mm in plane and 2–3 mm from plane to plane. This order of magnitude coarser resolution does not show breast architecture with the clarity available in X-ray mammograms that, nevertheless, are limited to showing only the X-ray absorption of tissue and the projection of 3-D architecture into two dimensions. In addition to being capable of isotropic high resolution, MRI has the inherent capability of showing weighted combinations of different tissue properties [19], [20], e.g., proton density, longitudinal relaxation time (typically denoted T1), and transverse relaxation time (typically denoted T2), by use of various pulse sequences and settings during data acquisition. These weighted combinations can allow visual recognition of tissue types. In addition, signal processing methods such as the analysis of principal components [21] can be used to segment the

NIH-PA Author Manuscript

NIH-PA Author Manuscript

NIH-PA Author Manuscript

volume into different types of tissues such as fat, connective tissue, ductal tissue, and fibroglandular tissue in breast.

Segmentation of medical images has been extensively investigated and, consequently, a number of processing techniques are available for use. See, for example, Refs. [22]–[26] for extensive treatments of segmentation in medical as well as nonmedical applications. In these treatments, the medical applications typically show the brain, heart chambers, a network of blood vessels, pulmonary pathways, and a skeleton of bones. The applications often exploit contrast difference between the structures being segmented and the background as well as knowledge of geometry. The application of interest here, i.e., to segment connective tissue from a background of fat in a reduction mammoplasty specimen, also uses a difference in contrast. For this application, a number of general techniques based on amplitude and geometry were investigated. The final selection of techniques and parameters resulted from a sequence of repeated trials driven by an expert knowledge of the morphology to be segmented.

Processing MRI data to obtain tissue morphology in a suitable form requires solution of three major problems. The first is that the MRI data may contain signal variation or shading that causes the same kind of tissue to have different amplitude values in different regions. The second is that some features of interest in the imaged volume are smaller than the MRI resolution and their representation is degraded by a so-called partial-volume effect that blurs the structure and reduces its contrast relative to the background. These two problems were solved in this investigation by a combination of initial processing, segmentation using different kinds of thresholding, and visualization using smoothed isosurfaces with transparency, lighting, shading, reflectance, and animation. The third problem is that different tissues may have similar MR responses. This problem was eliminated in this paper by restricting attention to a tissue specimen that was essentially comprised of two types of tissue, fat and connective tissue, that have readily distinguishable MR responses.

This investigation has two primary objectives. The first is to model tissue morphology in a form that is suitable for computation of ultrasound pulse-wave propagation in three dimensions. The second is to compute ultrasound pulse-wave propagation in three dimensions through the model. The described methods extend from two dimensions to three dimensions high-resolution large-scale modeling that allows comparison of calculated and measured data for improved understanding of ultrasound propagation in tissue, wavefront distortion resulting from the propagation, and methods for estimation of aberration.

The presentation is divided into sections. In Section II, the context and specific objectives for the selection of processing methods are outlined. The methods used in the study are summarized in Section III. Results of the study are shown in Section IV. In Section V, the methods and results are discussed. Conclusions are presented in Section VI.

II. Context and Objectives for Selection of Methods

A. Breast Composition and Morphology

The mature female breast has four main subcutaneous components: parenchyma (fibroglandular tissue), ducts, fat, and connective support [27]–[29], respectively. These components are organized into lobules that are grouped together into lobes. On average, a breast contains 15–20 lobes arranged roughly in a wheel-spoke pattern emanating from the region of the nipple. The distribution of the lobes is not even. Fibroglandular tissue dominates in the upper-outer portion of the breast. A tree-like structure of ducts spreads from the nipple through the lobes. The breast specimen used in this paper was obtained from reduction mammoplasty, a surgical procedure that removes fat and avoids the regions with

NIH-PA Author Manuscript

NIH-PA Author Manuscript

NIH-PA Author Manuscript

glandular tissue in young female breast. Therefore, the specimen mostly consisted of fat and connective tissue.

B. MRI Data Acquisition

The breast specimen used in this paper was frozen after surgical excision. The described methods are not currently applicable *in vivo* because clinical MRI scanners require impractically long scan times to obtain the required resolution for calculation of pulse-wave propagation. Before being scanned, the specimen was thawed and a portion cut to fit loosely in a rectangular plastic container with an inner cross section of 46×41 mm^2 and a depth of 41 mm. The container was filled with normal saline. Care was taken to avoid air bubbles in the container. The container was centered in a single-loop rectangular RF receiver volume coil made in-house and tuned to the proton resonance frequency at 3 T. The coil dimensions were $55 \times 50 \times 20$ mm^3, and resulted in a slip fit around the specimen container. The specimen–coil combination was centered in the bore of a 3 -T Siemens Trio MR imager. A 3-D gradient-echo pulse sequence called flz3d1 was employed to acquire a sequence of images with a resolution of 0.130×0.130 mm^2 from 320 consecutive planes separated by 0.150 mm. Each image spanned 49.92×49.92 mm^2, most of which was occupied by the specimen. However, in the third dimension, the specimen occupied only 160 planes that spanned an interval of 24.0 mm.

C. Pulse-Wave Propagation

The MRI data acquisition was configured to obtain a spatial resolution, sufficient for Nyquist sampling at the wavelength of the highest temporal frequency in the pulse wave that was subsequently propagated through the segmented breast. The temporal-frequency band of the pulse wave was selected to coincide with the pulse-wave parameters that are typically used in an available unique research ultrasound system [30] and to be in the range of clinical ultrasound systems used for diagnostic imaging. The values of the pulse parameters are given in Section III-E.

D. Image Processing Challenges

The selection of data processing methods was driven by the characteristics of the acquired MRI data. Although the in-plane and the plane-to-plane resolution was a small fraction of a millimeter, some features of interest were reduced in amplitude by partial-volume effects as illustrated in Fig. 1. Also, although a special RF coil was used to acquire data, the coil was relatively uncomplicated and resulted in the detected amplitude of the MR signal from the same kind of tissue varying from region to region throughout the imaged volume more than would have been the case if a phased array coil system were available. High resolution was obtained using the special receive coil with a long scanning time that lasted about 12 h. Because the scan time was long and scanner availability was limited, no attempt was made to calibrate inhomogeneity in the acquisition system. The systematic amplitude variation, or shading, is illustrated in Fig. 2. Mitigation of these effects along with the need to suppress noise motivated the selection of the preprocessing, segmentation, post-processing, and visualization methods used in this paper.

III. Methods

Segmentation and visualization of the MRI data consisted of four main steps. First, a nonlinear preprocessing filter was applied. Second, local and global thresholding were used for segmentation. Third, post-processing filters were applied to optimize visualization of the segmented data. Fourth, visualization was accomplished using isosurfaces that were rendered with lighting, shading, and reflectance. Image and video processing were performed using MATLAB [31], ImageJ [32], and VirtualDub [33].

NIH-PA Author Manuscript

NIH-PA Author Manuscript

NIH-PA Author Manuscript

A. Preprocessing (Nonlinear Smoothing)

Nonlinear spatial filtering was used to remove small details not of interest, to connect small gaps in features of interest, and to reduce noise. The filtering was performed on every voxel in the volume by using a multilevel bidirectional median filter [34]. This class of nonlinear filters operates on neighborhoods but, unlike linear filtering, the filtering operation is based conditionally on a statistic (i.e., the median) of voxel amplitudes in the neighborhood under consideration. The selection of a median type of filter for this study was made because this filter class has the desirable properties of reducing noise while preserving sharp edges.

Smoothing was performed independently on each cross section in the volume. Given that MED(A) represents the median value of set A, then, for each cross-sectional element $I_{j,k}$ where j and k are the index rows and columns in the cross section, respectively, the output of the multilevel bidirectional median filter was

$$\mathrm{MED}\left[\begin{array}{l} I_{j,k} \\ \mathrm{MED}\begin{pmatrix} I_{j,k}, I_{j+1,k}, I_{j+2,k} \\ I_{j-1,k}, I_{j-2,k}, I_{j,k+1} \\ I_{j,k+2}, I_{j,k-1}, I_{j,k-2} \end{pmatrix} \\ \mathrm{MED}\begin{pmatrix} I_{j,k}, I_{j+1,k+1}, I_{j+2,k+2} \\ I_{j-1,k-1}, I_{j-2,k-2}, I_{j+1,k-1} \\ I_{j+2,k-2}, I_{j-1,k+1}, I_{j-2,k+2} \end{pmatrix} \end{array}\right].$$

A Canny edge-detection filter [35] with a variance of 0.6 was applied to the cross sections after the nonlinear filtering operation to assess the effectiveness of noise reduction with preservation of edges and small details.

B. Segmentation

In the context of the present study, the goal of segmentation was to identify the connective tissue sheets that surround lobules of fat in the specimen. This goal was achieved using a combination of techniques in which voxels with an amplitude equal to or above a given value were assigned to the foreground class and voxels below the given value were assigned to the background class. Separate thresholding procedures were used to form binary images of fine detail and large features. These images were combined (i.e., added together) to form a single binary image of voxel classifications.

1) Thresholding for Large Features—Large features were identified by global segmentation of the image using Otsu's method to select the threshold [36]. In the Otsu's method, the threshold value is chosen to be the amplitude that results in the minimum of the interclass variance. Partial volume effects and local variations in the sensitivity of the MR imaging process can cause dropouts to occur in these binary images that thin boundaries and eliminate smaller objects.

2) Thresholding for Fine Detail—Fine detail lost in the segmentation of large features may be recovered by applying a threshold to the difference between the original image and the nonlinearly filtered image. Subtraction of the filtered image from the original image is equivalent to application of a high-pass filter that has the effect of emphasizing edges and small objects. The threshold value may, again, be chosen by the Otsu's method. In this study, however, the threshold value was chosen to be the mean value m of the amplitudes plus the standard deviation σ. Since the mean value of the data was 106 and the standard deviation was 10 when the data ranged from 0 to 255, the threshold for fine detail was 116.

NIH-PA Author Manuscript

NIH-PA Author Manuscript

NIH-PA Author Manuscript

This value is about 10% greater than the value of 105 yielded by the Otsu's method. The use of a threshold given by $m + \sigma$ produced better results than the threshold given by the Otsu's method.

Therefore, the implementation of the fine detail segmentation method in this study consisted of the following steps:

1. application of a multilevel bidirectional median filter to the original image;
2. subtraction of the filtered image from the original image;
3. segmentation of the difference image using a threshold given by $m + \sigma$;
4. inversion of the segmented image.

Finally, homogeneous subvolumes, known as objects [37], of the segmentation were found and those with a size smaller than 64 voxels were eliminated. A combination of the morphological procedures of dilation to grow structures and erosion to thin structures [37] was applied. Dilation improved continuity of the sheet-like membranes of connective tissue, and erosion suppressed artificial enhancement of subresolution features.

C. Visualization

Isosurfaces, smoothed by application of a Gaussian-shaped linear antialiasing filter that was based on a deformable level-set model [38], [39] using a kernel size of 5 × 5 × 5 voxels and a standard deviation of 0.5 voxels, were used in this study to visualize the volume of the segmented breast data [38] because the specimen in this study consisted of only two tissues, adipose tissue and connective tissue, respectively. However, because the structure of connective tissue is complex, specialized display techniques were used to enhance appreciation of the tissue architecture. These techniques consisted of transparency, lighting, shading, and animation [40]–[42]. Transparency values between 0 (totally opaque) and 1 (totally transparent) were tried. Lighting was employed with rays from sources positioned at azimuthal and polar angles of 80° and 130°, respectively. A Phong shading model [43] was used to characterize an isosurface by three types of light: ambient, diffuse, and specular, respectively. Values selected in this paper for Phong shading parameters were 0.3, 0.8, and 0, for the ambient, diffuse, and specular strengths, respectively.

After segmentation and visualization, the cross sections and volume animations were visually assessed for their verisimilitude. The assessment was used to adjust parameters in the segmentation and visualization. These adjustments consisted mostly of changes to show the connective tissue septa with an appropriate thickness and to reduce visualization artifacts in the isosurfaces.

D. Summary of the Steps Used to Process and Visualize the Breast Data

When all of the processing steps are combined, the following procedure is obtained:

1. visual inspection of MRI data;
2. interpolation to correct for the anisotropic resolution in the volume;
3. noise reduction using a multilevel bidirectional median filter;
4. segmentation using the described procedure that preserves fine detail;
5. labeling 3-D objects and elimination of very small objects;
6. application of dilation and erosion filters to connect gaps in surfaces;
7. visualization using isosurfaces, lighting, transparency, and animation;

NIH-PA Author Manuscript

NIH-PA Author Manuscript

NIH-PA Author Manuscript

8. assessment of the results.

In steps 3, 4, and 5, that require specification of the median-filter neighborhood size, the segmentation threshold, and the small object size, user interaction is needed. Nevertheless, guided segmentation is appropriate for this research-oriented tool. This interaction facilitates consultation with a breast pathologist to establish an essentially ideal correspondence of the model and histology.

E. Calculation of Ultrasound Propagation Through the Model

The segmented breast volume was used to construct an acoustic model of the breast specimen by assigning values of sound speed, density, and absorption to voxels corresponding to fat and connective tissue. In fat, the zero-frequency value of sound speed was 1.481 mm/μs, the target value of absorption was 1.3 dB/cm at 2.5 MHz, and the density was 0.950 g/mm^3. In connective tissue, the zero-frequency value of sound speed was 1.625 mm/μs, the target value of absorption was 4.0 dB/cm at 2.5 MHz, and the density was 1.120 g/mm^3. Two relaxation processes with relaxation times of 40 and 400 ns were assumed to govern the frequency-dependent relation between sound speed and absorption [44] that depends on the zero-frequency sound speed, target absorption, and density at each grid point. To avoid calculating and storing these frequency-dependent compressibilities at each grid point, a time-saving approximation was adopted. Reference values of zero-frequency sound speed, absorption, and density were calculated from volume-fraction-weighted averages over the medium. The reference values were used to compute a single pair of frequency-dependent compressibilities that were used to determine the frequency-dependent compressibility in each voxel by scaling the reference values depending on the values of zero-frequency sound speed, target absorption, and density in each voxel. The breast phantom was resampled using nearest-neighbor interpolation to obtain an isotropic resolution of 75 μm, padded with a zero-absorption fat-like boundary, the same size as the 10-voxel-wide perfectly matched layer (PML) [45] (with nonzero attenuation to suppress reverberations), and then smoothed using half-band filtering [46] to band limit the spatial-frequency content of the medium variations. The resolution was selected to satisfy sampling requirements for propagation of a time-domain pulse with a center frequency of 2.5 MHz and a −6-dB bandwidth of 1.7 MHz. A point source was positioned outside of the computational domain to eliminate the need to accommodate a singularity, and ultrasound wave propagation through the medium was calculated.

The calculation was performed using a 3-D finite-difference time-domain *k*-space method [12] using a time step of 20 ns (Courant–Friedrichs–Lewy number~0.4). The breast model after resampling and padding filled a 557 × 451 × 289 3-D grid and required nearly one gigabyte of storage. This large scale along with computational demands of the 3-D fast Fourier transform used to calculate spatial derivatives were satisfied by performing the calculation on a cluster of computers. The cluster [47] consisted of 672 cores with 24-TB storage, 1.3-TB RAM, and a peak performance of approximately 7 Tflops, communicating over a Gb/s Ethernet. Compute nodes each contained two 3.0-GHz quad-core Xeon processors, 16-GB RAM, and 73 GB of local storage. Propagation through the model was executed on 64 cores spread over 32 nodes and required 24 h.

The wave field was sampled in three orthogonal planes at each temporal iteration. Two observation planes contained the centrally located origin. The third plane was offset from the origin to the edge of the computational domain just inside the PML to represent a receiving aperture. Time-domain waveforms in the offset plane segment were processed to appear as if they were sampled at 20 MHz in the aperture of a 57 × 57 2-D transducer array with a 0.6-mm pitch, choices motivated by the dimension of the specimen and the specifications of the previously referenced ultrasound system [30]. The transducer

NIH-PA Author Manuscript

NIH-PA Author Manuscript

NIH-PA Author Manuscript

waveforms were corrected for geometry associated with the apparent point source location and used to estimate arrival-time and energy-level fluctuations. The arrival-time fluctuation at any given position was defined as the shift in arrival time of the echo at the position relative to a reference position, chosen to be the center position in the reported calculations. These fluctuations were calculated by cross-correlating waveforms received at neighboring elements because echos from a point appear coherent over a length scale that is several times smaller than the correlation length of the aberration. The energy-level fluctuation at any given position was defined as the difference in energy of echos received at the position relative to a reference position, again chosen to be the center position in the reported calculations. Details of the methods used for calculating arrival-time and energy-level fluctuations can be found in [3]

A video sequence showing the calculated propagation of the pulse wave through the three orthogonal planes was made.

IV. Results

The results of noise reduction using a simple median filter and a multilevel bidirectional median filter are illustrated in Fig. 3. The cross section that was filtered with a 5 × 5-pixel simple median filter shows a greater loss of detail and edges than the cross section that was filtered with a multilevel bidirectional median filter having the same span. As is evident in the figure, application of a Canny edge-detection filter emphasizes this difference between the results obtained with the two nonlinear smoothing filters.

Illustrative results of segmentation based on global thresholding are shown in Fig. 4. The segmentation was performed after noise reduction using the described multilevel bidirectional median filter. The images show the sensitivity to the values of the threshold and shading results in unsatisfactory segmentation using a single histogram-based threshold.

Segmentation based on the described procedure that preserves fine detail is shown in Fig. 5. In this figure, the difference image was segmented with a threshold value that was chosen heuristically. The contour showing the edge of the specimen has been removed because this contour is unrelated to the intrinsic morphology of the specimen. The sequence of steps used to process the breast data is summarized in Fig. 6.

The results of Gaussian smoothing shown in Fig. 7 and the results of transparency adjustments shown in Fig. 8 depict morphology comprehensibly.

The different views shown in Fig. 9 facilitate further appreciation of the structure. Animation that shows the segmented specimen from a sequence of viewing angles also improves appreciation. This is illustrated in a video that can be seen on a Web site [48]. In the video, two rotations are used, one around a vertical axis and the other around a horizontal axis, to present the segmented specimen from different viewing angles.

Ultrasound pulse-wave propagation through the segmented breast specimen is shown in orthogonal planes at three representative instants in Fig. 10. Because the entire medium, excluding the PML, is different from the background, scattered waves appear even in the absence of discontinuities in density, compressibility, and absorption. The complete video sequence of the propagation of the pulse wave is shown in a video that can be seen on a Web site [49].

A subset of waveforms across columns of the simulated aperture is shown in Fig. 11. Time shifts and amplitude variations as well as wavefront spreading are all evident. No amplitude compensation is applied to the waveforms and because the point source is directly below the

NIH-PA Author Manuscript

NIH-PA Author Manuscript

NIH-PA Author Manuscript

center of the array, the amplitudes of the received waves are greater at the center of the array. Calculations of arrival-time fluctuation and energy-level fluctuation statistics in the central 34.2 × 34.2-mm^2 portion of the offset plane are shown in Fig. 12. As shown in Table I, all the statistics computed from calculated propagation agree well with statistics from measurements reported in [4] for specimens of human breast with comparable thickness and morphology.

V. Discussion

A. Segmentation

Trials were performed to remove shading in the MRI data set by using the rolling ball algorithm [50] and homomorphic filtering [51]. Neither method was satisfactory. Results of these trials and comparisons with the methods described in the present report are in [52]. As also shown in [52], trials with single-level median filtering were ineffective compared to multilevel bidirectional median filtering for simultaneous noise reduction and edge preservation. Furthermore, algorithms such as global thresholding [37], snake [53], livewire [54], and watershed [37] performed poorly with the shading present in the MRI data used in this study. Segmentation based on a procedure that preserves fine detail reduced the effects of shading. [52] A limitation of segmentation procedures that preserve fine detail is, however, that large features are lost. This limitation was overcome by use of the Otsu's method. In general, the combination of the special procedure for segmenting fine detail and the Otsu's method of thresholding satisfactorily segmented the breast data in this study.

B. Visualization

Direct visualization of binary volumes resulted in aliasing artifacts. Application of a 3-D Gaussian smoothing filter suppressed aliasing and produced surfaces consistent with known morphology of adipose and connective tissues in breast. 3-D visualization of complex structures was enhanced by use of transparency, lighting, shading, and object reflectance. Lighting proved to be the most important of all these techniques.

The described segmentation and visualization methods have other applications beyond their use for calculation of ultrasound propagation to characterize aberration. The methods, for example, may be used to facilitate understanding of complex abnormal morphology of other tissues or separate blood vessels (veins, arteries, and capillaries) in fluorescence microscopy. The methods can also be directly extended to additional tissue classes through recursive application of the methods. However, for any specific clinical application, parameters of the methods need to be adjusted during review by a morphologist. After this, the parameters may be suitable for a series of scans under the same conditions.

Because the small and subresolution features are difficult to segment, imaging the breast specimen with higher resolution would facilitate segmentation and improve the results. Additionally, use of a phased array of RF coils to give a more uniform amplitude of the same structures throughout the field of view would lessen the need for user interaction and facilitate automation of the processing. Use of different MRI pulse sequences coupled with so-called fat and water suppression is likely a worthwhile way to improve quality of the MRI data.

C. Propagation

The segmentation produces a model of breast with features on a scale larger than about 150 μm. This scale allowed accurate calculation of wave propagation in spite of subresolution features in the specimen. The subresolution inhomogeneities that predominated in the studied specimen are collagenous membranes that support clusters of fat cells. Fat cells have

NIH-PA Author Manuscript

NIH-PA Author Manuscript

NIH-PA Author Manuscript

a typical maximum size of about 80 μm [55] and the collagenous membranes are expected to be no more than 5 μm thick. The total power scattered by these subresolution inhomogeneities is much smaller than the total power scattered by the resolved inhomogeneities and contributes to a loss that is accounted for in calculations by relaxation absorption. Because the properties of the tissues in the model are derived [9] from studies of bulk tissues that also contain the subresolution inhomogeneities, their effect is included by basing the parameter selection on measured properties of tissues. Additionally, since subresolution scattering has low amplitude, absorption suppresses this component. If a subresolution feature is smaller in extent than a single voxel, elevating the feature to a full voxel is inappropriate because scattering at that scale is proportional to the volume of the scatterer [56]. This artificial enhancement of the scattering amplitude is further enhanced by half-band filtering required to band limit the spatial-frequency content of the segmented breast.

Aberration estimated and shown in Fig. 12 is along paths to the point source. Aberration of the wavefront is comprised of fluctuations in both arrival time and energy level. These fluctuations have magnitudes that are much greater than both time and amplitude increments used in current b-scan imaging instrument beamformers. The aberration can, therefore, severely degrade focusing with the result that point and contrast resolution are poorer than would be obtained in a homogeneous medium. The intuition that time shifts are caused by sound speeds that differ in the path of one part of the wavefront from the path of another part of the wavefront is confirmed by observation of the wavefront [49] as it propagates through the model. The less intuitive presence of changes in amplitude is explained by observing that the path-dependent diffraction and scattering differ from one part of the wavefront to another, particularly, when the wavefront propagates along the length of the inhomogeneity rather than across the inhomogeneity. Compensation for both forms of aberration is necessary to improve focusing in current b-scan imaging and also to obtain the full benefit of resolution improvement that can be realized from the use of expanded apertures.

Although the estimated aberration is associated with a single point, the estimate can be used to compensate for aberration in an entire isoplanatic patch, i.e., the region surrounding the location of an ideally formed point source (or focus) throughout which a single estimate of aberration can be used for compensating transmissions and receptions [57]. Since the size of this region depends on the nature of the aberration or propagation path, recalculation of aberration for point sources in a neighborhood would allow determination of the size of the isoplanatic patch.

The method used to estimate arrival-time fluctuations shown in Fig. 12 uses waveforms that are corrected for an apparent source location. Because the source location is estimated, only relative shifts in arrival time can be calculated. This prohibits an absolute calculation of the average sound speed in the tissue that may otherwise be used to characterize the type of tissue in the propagation path.

In Table I, where simulated and measured breast aberration statistics are compared, remarkable agreement is seen in the arrival-time fluctuations. Energy-level fluctuations in the simulations are only slightly less than the measured values.

Averaging by reception with a “large” element smooths the aberration at the element [58]. This highlights the need for appropriately sized elements in an ultrasound system that is capable of estimating and correcting the aberration. The reported *k*-space calculations of propagation used a spatial step size of 75 μm. Therefore, aberrator correlation lengths on a similar scale can be detected. Although the element pitch used in the simulated aperture was

NIH-PA Author Manuscript

NIH-PA Author Manuscript

NIH-PA Author Manuscript

0.6 mm, the aggregation of received signals over smaller element sizes did not significantly change the measured aberration. This is because the correlation length of the aberration was several times the 0.6 mm pitch used to aggregate received signal. Therefore, the simulated element size was appropriate for the model.

Most current clinical ultrasound systems are capable of transmission at a fundamental center frequency and reception around the second harmonic of the fundamental frequency. The harmonics are produced by nonlinear propagation of the fundamental band of frequencies. Because the harmonic wave builds during propagation, some one-way effects of aberration are reduced by forming images using the harmonic reflections. However, localization of the sources of the harmonic reflections still depends somewhat upon high-quality focusing of the fundamental-band transmission and also on high-quality receive focusing of the harmonic waves that, because the wavelengths are shorter, are even more perturbed by the same scale of inhomogeneities that affect the fundamental-band waves. Since previous studies [59] have shown near-water-path restoration of focusing, and the methods can be applied to reception by using frequency translation at the scattering structures, the methods can be employed to investigate aberration estimation and correction in harmonic imaging as well.

The methods that are presented in this paper can be used for further studies that go beyond the scope of the current presentation. The methods can be used as a test bed for reproducible studies of aberration-correction techniques. Images can be formed with and without estimation and correction of aberration. In these images, contrast ratios calculated for objects, such as cysts, can serve as performance metrics for the imaging algorithms. When the model and 3-D propagation algorithms are used for calculations of transmit focusing with uncompensated and compensated beams, the transmit beam width at the focus will be another performance metric.

VI. Conclusion

Data obtained from high-resolution MRI is ideal for modeling tissue morphology for applications such as ultrasound wave propagation studies.

The presented semi-automatic algorithm for expert-guided segmentation of high-resolution MRI data resulted in a model of human breast with acoustic properties comparable to those measured experimentally. For the dataset in this study, nonlinear smoothing with a multilevel bidirectional filter worked well to remove image noise and to preserve edges. A combination of thresholding for fine detail and thresholding for large features performed well as a segmentation technique to mitigate the effects of shading in the dataset. Application of morphologic filters to the segmented volume enhanced the segmentation. Overall, the results show the feasibility of using high-resolution MRI coupled with preprocessing, segmentation, post-processing, and visualization to depict the morphology of breast tissue for the study of ultrasound propagation in the breast.

Excellent agreement between calculated and measured properties of waveforms received in an aperture bolster confidence in the verisimilitude of the model and accuracy of the methods. The current study lays a foundation upon which further studies can be based. In particular, newly emerging clinical ultrasound systems already incorporate 2-D arrays of elements but lack the capability to estimate and correct aberration. The combination of the methods in this paper is suitable for testing aberration estimation and correction techniques for their expeditious incorporation into clinical systems.

NIH-PA Author Manuscript

NIH-PA Author Manuscript

NIH-PA Author Manuscript

Acknowledgments

The authors would like to thank the Ultrasound Research Laboratory team, J. P. Astheimer, A. J. Hesford, D. P. Duncan, J. Jin, and W. Jiang, for useful discussions throughout the course of this research.

The authors would also like to thank J. Zhong for advice in the general area of MRI and E. Kwok for designing the coil and acquiring the MRI data used in this study.

This work was supported by the National Institutes of Health under Grant EB000280 and the University of Rochester Diagnostic Ultrasound Research Laboratory Industrial Associates.

References

1. Hagen-Ansert, SL. Textbook of Diagnostic Ultrasonography. 6. Vol. 1 & 2. St. Louis, MO: C. V. Mosby; 2006.
2. Rumack, C.; Wilson, S.; Charboneau, JW.; Johnson, J. Diagnostic Ultrasound. 3. St. Louis, MO: C. V. Mosby; 2004.
3. Hinkelman LM, Liu DL, Metlay LA, Waag RC. Measurements of ultrasonic pulse arrival time and energy level variations produced by propagation through abdominal wall. J Acoust Soc Amer 1994;95(1):530–541. [PubMed: 8120264]
4. Hinkelman LM, Liu DL, Waag RC, Zhu Q, Steinberg BD. Measurement and correction of ultrasonic pulse distortion produced by the human breast. J Acoust Soc Amer 1995;97(3):1958–1969. [PubMed: 7699176]
5. Mast TD, Hinkelman LM, Orr MJ, Sparrow VW, Waag RC. Simulation of ultrasonic pulse propagation through the abdominal wall. J Acoust Soc Amer 1997;102(2):1177–1190. [PubMed: 9265762]
6. Mast TD, Hinkelman LM, Metlay LA, Orr MJ, Waag RC. Simulation of ultrasonic pulse propagation, distortion, and attenuation in the human chest wall. J Acoust Soc Amer 1999;106(6):3665–3677. [PubMed: 10615705]
7. Tabei M, Mast TD, Waag RC. Simulation of ultrasonic focus aberration and correction through human tissue. J Acoust Soc Amer 2003;113(2):1166–1176. [PubMed: 12597210]
8. Hinkelman LM, Metlay LA, Churukian CJ, Waag RC. Modified gomori trichrome stain for macroscopic tissue slices. J Histotechnol 1996;19(4):321–323.
9. Duck, FA. Physical Properties of Tissue: A Comprehensive Reference Book. London, U.K: Academic; 1990.
10. Goss SA, Johnston RL, Dunn F. Comprehensive compilation of empirical ultrasonic properties of mammalian tissues. J Acoust Soc Amer 1978;64(2):423–457. [PubMed: 361793]
11. Goss SA, Johnston RL, Dunn F. Compilation of empirical ultrasonic properties of mammalian tissues. II. J Acoust Soc Amer 1980;68(1):93–108. [PubMed: 11683186]
12. Tillett JC, Daoud MI, Lacefield JC, Waag RC. A *k*-space method for acoustic propagation using coupled first-order equations in three dimensions. J Acoust Soc Amer 2009;126(3):1231–1244. [PubMed: 19739736]
13. Hesford AJ, Astheimer JP, Greengard LF, Waag RC. A mesh-free approach to acoustic scattering from multiple nested spherical objects using Rokhlin's diagonal form for partial wave expansions. J Acoust Soc Amer 2009;127(2):850–861. [PubMed: 20136208]
14. Mamou J, Oelze ML, O'Brien JWD, Zachary JF. Identifying ultrasonic scattering sites from 3D impedance maps. J Acoust Soc Amer 2005;117(1):413–423. [PubMed: 15704434]
15. Mamou J, Oelze ML, O'Brien JWD, Zachary JF. Extended three-dimensional impedance map methods for identifying ultrasonic scattering sites. J Acoust Soc Amer 2008;123(2):1195–1208. [PubMed: 18247919]
16. Visible Human Project. 2010 Mar 2. [Online]. Available: WWW http://www.nlm.nih.gov/research/visible/visible_human.html
17. Mast TD. Two- and three-dimensional simulations of ultrasonic propagation through human breast tissue. Acoust Res Lett Online 2002;3(2):53–58.

NIH-PA Author Manuscript

NIH-PA Author Manuscript

NIH-PA Author Manuscript

18. Aroyan JL. Three-dimensional modeling of hearing in delphinus delphis. J Acoust Soc Amer 2001;110(6):3305–3318. [PubMed: 11785831]
19. Webb, A. Introduction to Biomedical Imaging. Hoboken, NJ: Wiley; 2003.
20. Westbrook, C.; Roth, CK.; Talbot, J. MRI in Practice. Malden, MA: Blackwell; 2005.
21. Jolliffe, IT. Principal Component Analysis. 2. New York: Springer-Verlag; 2002.
22. Pham DL, Xu C, Prince JL. Current methods in medical image segmentation. Annu Rev Biomed Eng 2000;2:315–337. [PubMed: 11701515]
23. Sonka, M.; Fitzpatrick, JM. Medical Image Processing and Analysis. Vol. 2. Bellingham, WA: SPIE; 2000. Handbook of Medical Imaging.
24. Sonka, M.; Hlavac, V.; Boyle, R. Image Processing, Analysis, and Machine Vision. 3. Toronto, Canada: Thompson Learning; 2007.
25. Liew AWC, Hong H. Current methods in the automatic tissue segmentation of 3D magnetic resonance brain images. Curr Med Imag Rev 2006;2(1):1–13.
26. Zhang, Y-J. Advances in Image and Video Segmentation. Hershey, PA: IRM Press; 2006.
27. Gray, H. Anatomy of the Human Body. Vol. 1918. Philadelphia, PA: Lea & Febiger; 2000.
28. Netter, FH. The Ciba Collection of Medical Illustrations: Reproductive System. 5. Vol. 2. Caldwell, NJ: Ciba; 1974.
29. Clemente, CD. Anatomy: A Regional Atlas of the Human Body. 5. Philadelphia, PA: Lippincott, Williams, & Wilkins; 2007.
30. Lacefield JC, Waag RC. Time-shift estimation and focusing through distributed aberration using multirow arrays. IEEE Trans Ultrason, Ferroelectr, Freq Control Nov;2001 48(6):1606–1624. [PubMed: 11800123]
31. MATLAB. 2010 Mar 2. [Online]. Available: WWW http://www.mathworks.com
32. ImageJ Image Processing and Analysis in Java. 2010 Mar 2. [Online]. Available: WWW http://rsb.info.nih.gov/ij/
33. VirtualDub. 2010 Mar 2. [Online]. Available: WWW http://www.virtualdub.org/index.html
34. Nieminen A, Heinonen P, Neuvo Y. A new class of detail-preserving filters for image processing. IEEE Trans Pattern Anal Mach Intell Jan;1987 PAMI-9(1):74–90.
35. Canny J. A computational approach to edge detection. IEEE Trans Pattern Anal Mach Intell Nov; 1986 PAMI-8(6):679–698.
36. Otsu N. A threshold selection method from gray-level histograms. IEEE Trans Syst Man Cybern A Syst Humans Jan;1979 9(1):62–66.
37. Gonzales, RC.; Woods, RE.; Eddins, SL. Digital Image Processing. 2. Vol. ch 9–10. Upper Saddle River, NJ: Prentice-Hall; 2002.
38. Whitaker, RT. Isosurfaces and Level Sets. Hansen, CD.; Johnson, CR., editors. San Diego, CA: Academic; 2005. p. 97-123.
39. Whitaker RT. Reducing aliasing artifacts in isosurfaces of binary volumes. Proc IEEE Vol Vis Graph Symp 2000:23–32.
40. Kniss JM, Premoze S, Hansen C, Ebert D. Interactive translucent volume rendering, and procedural modeling. Proc IEEE Vis 2002:109–116.
41. Silva CT, Comba JLD, Callahan SP, Bernardon FF. A survey of gpu-based volume rendering of unstructured grids. Revista de Informatica Teorica e Aplicada 2005;12(2):9–29.
42. Fleming RW, Dror RO, Adelson EH. Real-world illumination, and the perception of surface reflectance properties. J Vis 2003;3(5):347–368. [PubMed: 12875632]
43. Phong BT. Illumination for computer generated pictures. Comm ACM 1975;18(6):311–317.
44. Nachman AI, Smith JF, Waag RC. An equation for acoustic propagation in inhomogeneous media with relaxation losses. J Acoust Soc Amer 1990;88(3):1584–1595.
45. Berenger JP. A perfectly matched layer for the absorption of electromagnetic waves. J Comput Phys 1994;114(2):185–200.
46. Crochiere, RE.; Rabiner, LR. Multirate Digital Signal Processing. Englewood Cliffs, NJ: Prentice-Hall; 1983. p. 155-157.

NIH-PA Author Manuscript

NIH-PA Author Manuscript

NIH-PA Author Manuscript

47. Center for Research Computing. 2010 Mar 2. [Online]. Available: WWW http://www.crc.rochester.edu/

48. Segmented Breast. 2010 Mar 2. [Online]. Available: WWW http://www.ece.rochester.edu/projects/ultrasoundres/BreastVisualization.mpg

49. Scattering by Breast. 2010 Mar 2. [Online]. Available: WWW http://www.ece.rochester.edu/projects/ultrasoundres/ScatteringByBreast.mpg

50. Sternberg, S. Computer. Vol. 16. Jan. 1983 Biomedical image processing; p. 22-34.

51. Pratt, WK. Digital Image Processing. 3. Hoboken, NJ: Wiley; 2001.

52. Salahura, G. Master's thesis. Dept. Electr. Comput. Eng., Univ. Rochester; Rochester, NY: Dec. 2006 Three-dimensional segmentation of breast sequential cross sections for studies of ultrasonic propagation.

53. Kass M, Witkin A, Terzopoulos D. Snakes – active contour models. Int J Comput Vis 1987;1(4): 321–331.

54. Mortensen EN, Barrett WA. Interactive segmentation with intelligent scissors. Graph Model Imag Process 1998;60(5):349–384.

55. Guo W, Bigornia S, Leizerman I, Xie W, McDonnell M, Clemente K, Pirtskhalava T, Kirkland JL, Gokce N, Corkey BE, Sullivan LM, Apovian CM. New scanning electron microscope method for determination of adipocyte size in humans and mice. Obesity 2007;15(7):1657–1665. [PubMed: 17636083]

56. Morse, PM.; Ingard, KU. Theoretical Acoustics. Vol. Ch 8. New York: McGraw-Hill; 1968.

57. Pilkintgton, WC. PhD thesis. Dept. Electr. Comput. Eng., Univ. Rochester; Rochester, NY: 2005. Isoplanatic patch size for aberration correction in ultrasonic imaging.

58. Liu DLD. Element size effect on phase aberration correction. IEEE Trans Ultrason, Ferroelect, Freq Contr Sep;2002 49(9):1212–1221.

59. Waag RC, Astheimer JP. Statistical estimation of ultrasonic propagation path parameters for aberration correction. IEEE Trans Ultrason, Ferroelectr, Freq Control May;2005 52(5):851–869. [PubMed: 16048187]

NIH-PA Author Manuscript
NIH-PA Author Manuscript
NIH-PA Author Manuscript

Biographies

Gheorghe Salahura was born in Breaza, Suceava county, Romania, on April 8, 1974. He received the B.E. and M.E. degrees in electrical engineering from Gheorghe Asachi Technical University, Iasi, Romania, in 1998 and 1999, respectively, and the M.Sc. degree in electrical engineering from University of Rochester, Rochester, NY, in 2007.

From 2007 to 2009, he was a Visiting Research Associate in the Ultrasound Research Laboratory, University of Rochester. Since 2009, he has been a Laboratory Technician in

NIH-PA Author Manuscript

NIH-PA Author Manuscript

NIH-PA Author Manuscript

the Center for Neural Development and Disease, University of Rochester Medical Center. His current research interests include signal and image processing and visualization.

Mr. Salahura is a member of the IEEE Engineering in Medicine and Biology Society.

Jason C. Tillett (M'10) received the B.S. degree in physics and astronomy from the University of Rochester, Rochester, NY, in 1986, and the Ph.D. degree in physics from the University of Delaware, Newark, in 1992.

NIH-PA Author Manuscript

NIH-PA Author Manuscript

NIH-PA Author Manuscript

After completing his Ph.D., he founded a small Internet Service Provider that he left to accept a fellowship at the Rochester Institute of Technology. Since 2004, he has been a Research Associate in the Ultrasound Research Laboratory, University of Rochester. His current research interests include experimental ultrasound imaging with aberration correction and large-scale calculations of wave propagation using high-performance computing.

Dr. Tillett is a member of the Acoustical Society of America and the American Institute for Ultrasound in Medicine.

Leon A. Metlay received the B.A. degree (Hons.) in chemistry from Swarthmore College, Swarthmore, PA, in 1973, and the M.D. degree from the University of Pittsburgh, Pittsburgh, PA, in 1977.

After completing a residency in anatomic and clinical pathology in 1981, he spent a year as a Pathologist at Pittsburgh's Oakland VA Hospital. In 1982, he joined the University of Rochester, Rochester, NY, where he is currently a Clinical Associate Professor of pathology and laboratory medicine in the Department of Pathology and Laboratory Medicine. He was engaged in research on perinatal diseases and has also been actively involved in providing morphologic correlation for imaging scientists.

Dr. Metlay is a Fellow of the College of American Pathologists and active in the Society for Pediatric Pathology. He was a receipient of the Keith Miner Ford Award from the University of Rochester for excellence in teaching and the Alumni Association Gold Medal Award for devotion to medical students in 2009.

Robert C. Waag (LF'03) received the B.E.E. and M.S. degrees in electrical engineering, and the Ph.D. degree in communications engineering, all from Cornell University, Ithaca, NY, in 1961, 1963, and 1965, respectively.

He was a Member of the technical staff at Sandia Laboratories, Albuquerque, NM, and then, served as an Officer in the United States Air Force from 1966 to 1969 at the Rome Air Development Center, Griffiss Air Force Base, NY. In 1969, he joined the faculty of the University of Rochester, Rochester, NY, where he is currently an Arthur Gold Yates Professor in the Department of Electrical and Computer Engineering, School of Engineering and Applied Science, and also holds an appointment in the Department of Imaging Sciences,

NIH-PA Author Manuscript

NIH-PA Author Manuscript

NIH-PA Author Manuscript

School of Medicine and Dentistry. His current research interests include ultrasonic scattering, propagation, and imaging in medical applications.

Prof. Waag received the Joseph H. Holmes Pioneer Award from the American Institute of Ultrasound in Medicine in 1992. He is a Fellow of the Acoustical Society of America and the American Institute of Ultrasound in Medicine.

NIH-PA Author Manuscript

NIH-PA Author Manuscript

NIH-PA Author Manuscript

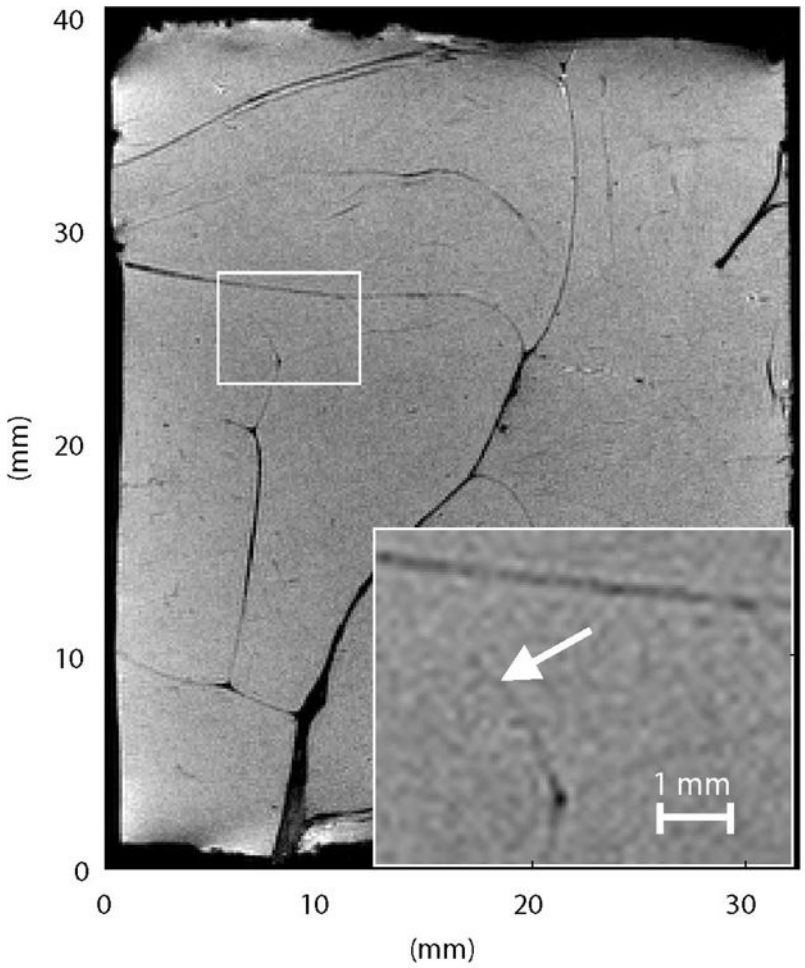

Fig. 1.

Illustration of partial volume effect. The small rectangle in upper left shows a portion of the cross section with small features that are not entirely resolved during the imaging process. This is more visible in the larger rectangle that is a 3× magnification of the small rectangle. The white arrow points to a feature that is barely visible.

NIH-PA Author Manuscript
NIH-PA Author Manuscript
NIH-PA Author Manuscript

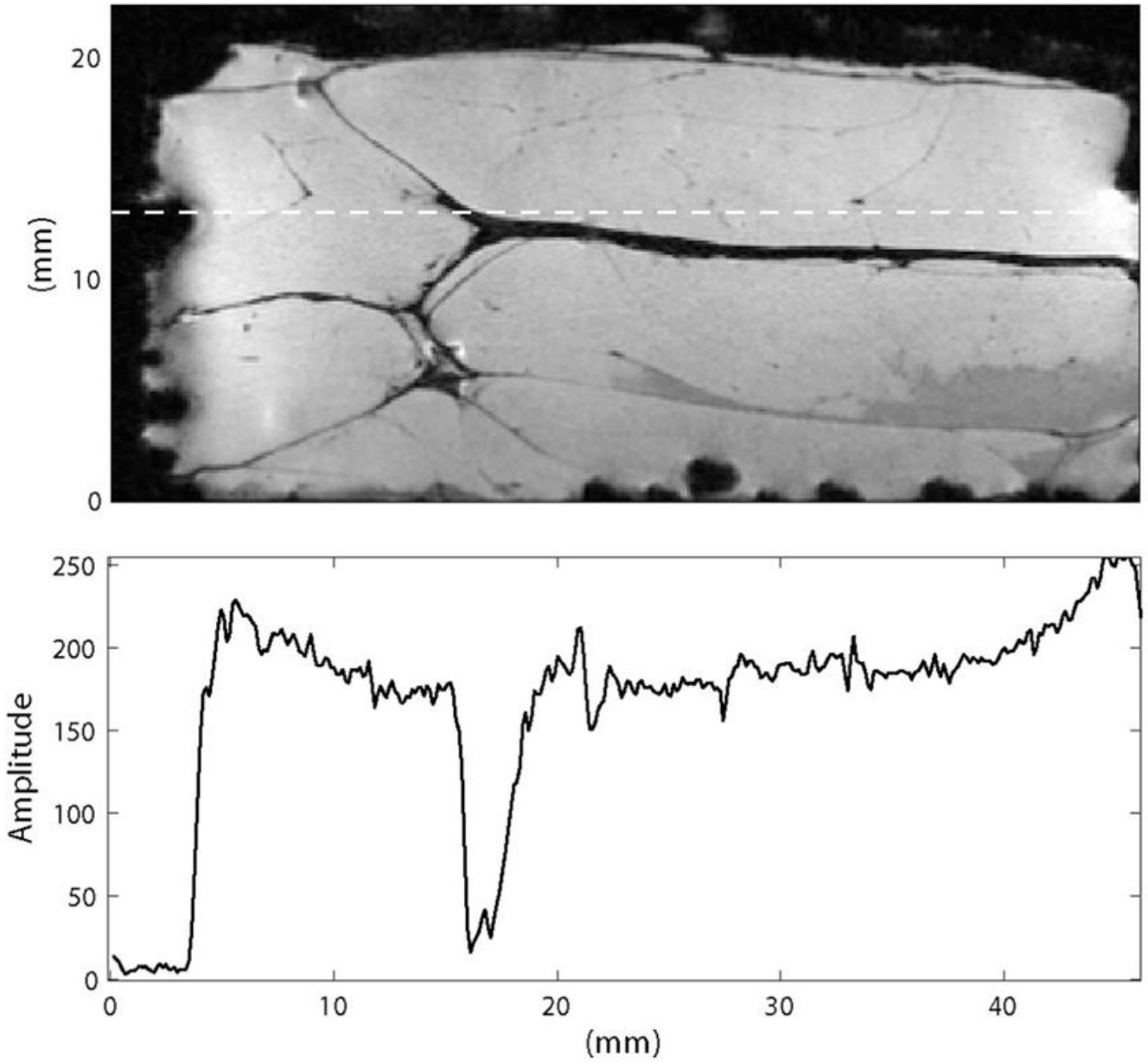

Fig. 2.
Amplitude shading. The top panel shows an MR cross section with a shading artifact. The bottom panel shows an amplitude profile along the white horizontal line on the cross section in the upper panel. The nonuniformity of amplitudes is clearly seen in both panels.

NIH-PA Author Manuscript
NIH-PA Author Manuscript
NIH-PA Author Manuscript

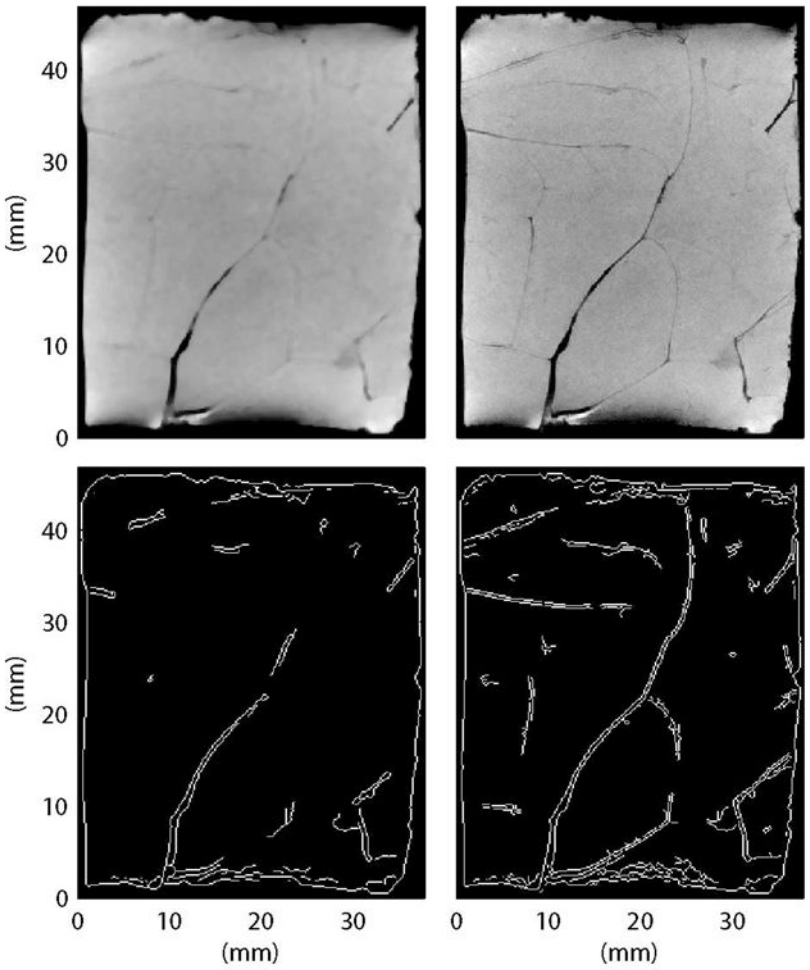

Fig. 3.

Illustration of noise reduction using a simple median filter and using a multilevel bidirectional median filter, each with a 5 × 5-span. The top-left and top-right panels show cross sections after application of a simple median filter and of a multilevel bidirectional median filter, respectively. The panels in the bottom show the result of applying a Canny edge detection filter to the cross sections shown on top. The variance for the Canny filter was chosen 0.6 for each cross section.

NIH-PA Author Manuscript
NIH-PA Author Manuscript
NIH-PA Author Manuscript

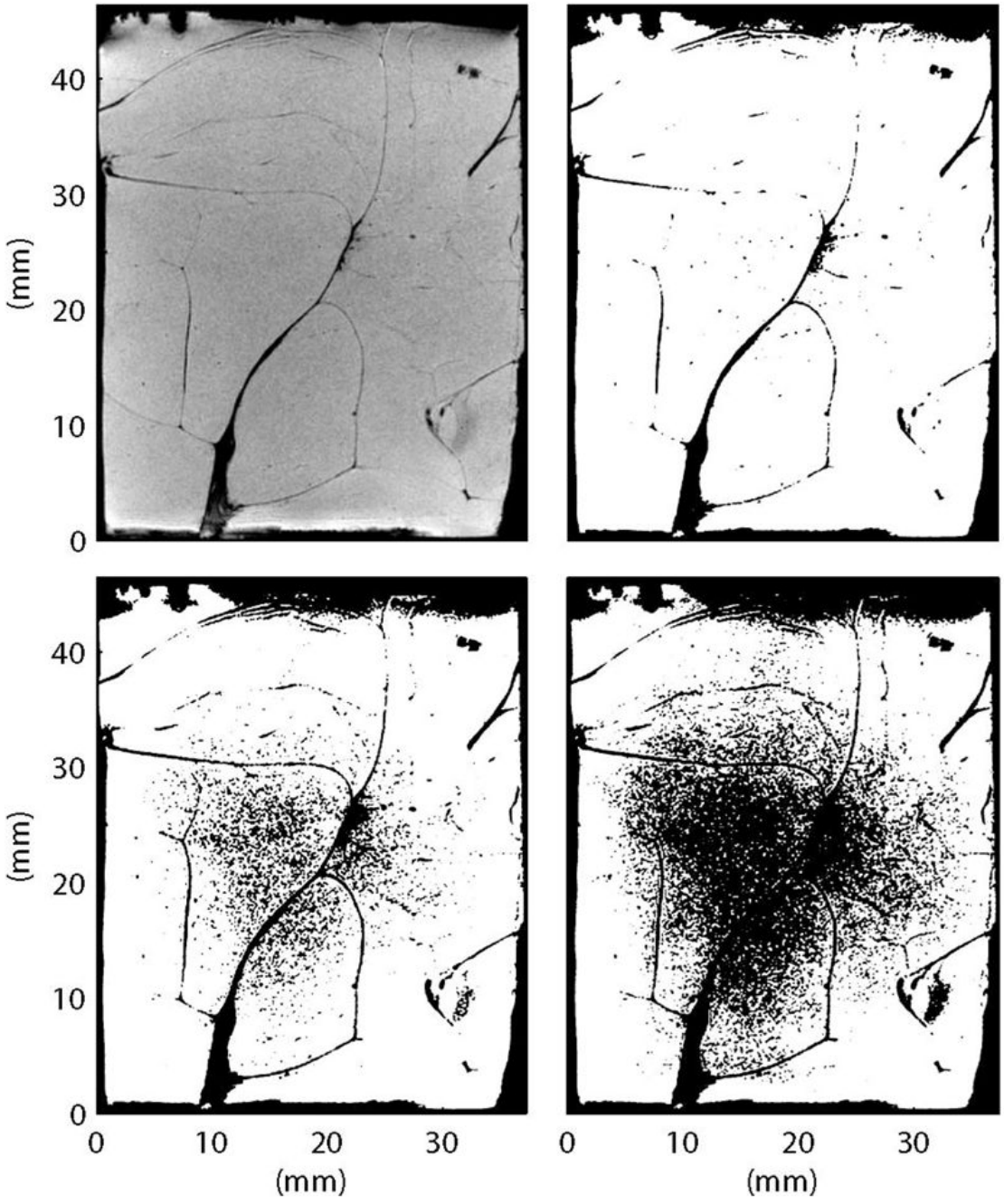

Fig. 4.

Segmentation based on histogram thresholding. The top left panel shows a cross section after application of a 5 × 5 multilevel bidirectional median filter. The top-right panel shows the cross section after segmentation using an amplitude threshold value of 110 on a scale of 0–255. The bottom-left and bottom-right panels show the cross section after segmentation using thresholding values of 128 and 140, respectively. The effects of shading on segmentation are most apparent in the lower right panel.

NIH-PA Author Manuscript
NIH-PA Author Manuscript
NIH-PA Author Manuscript

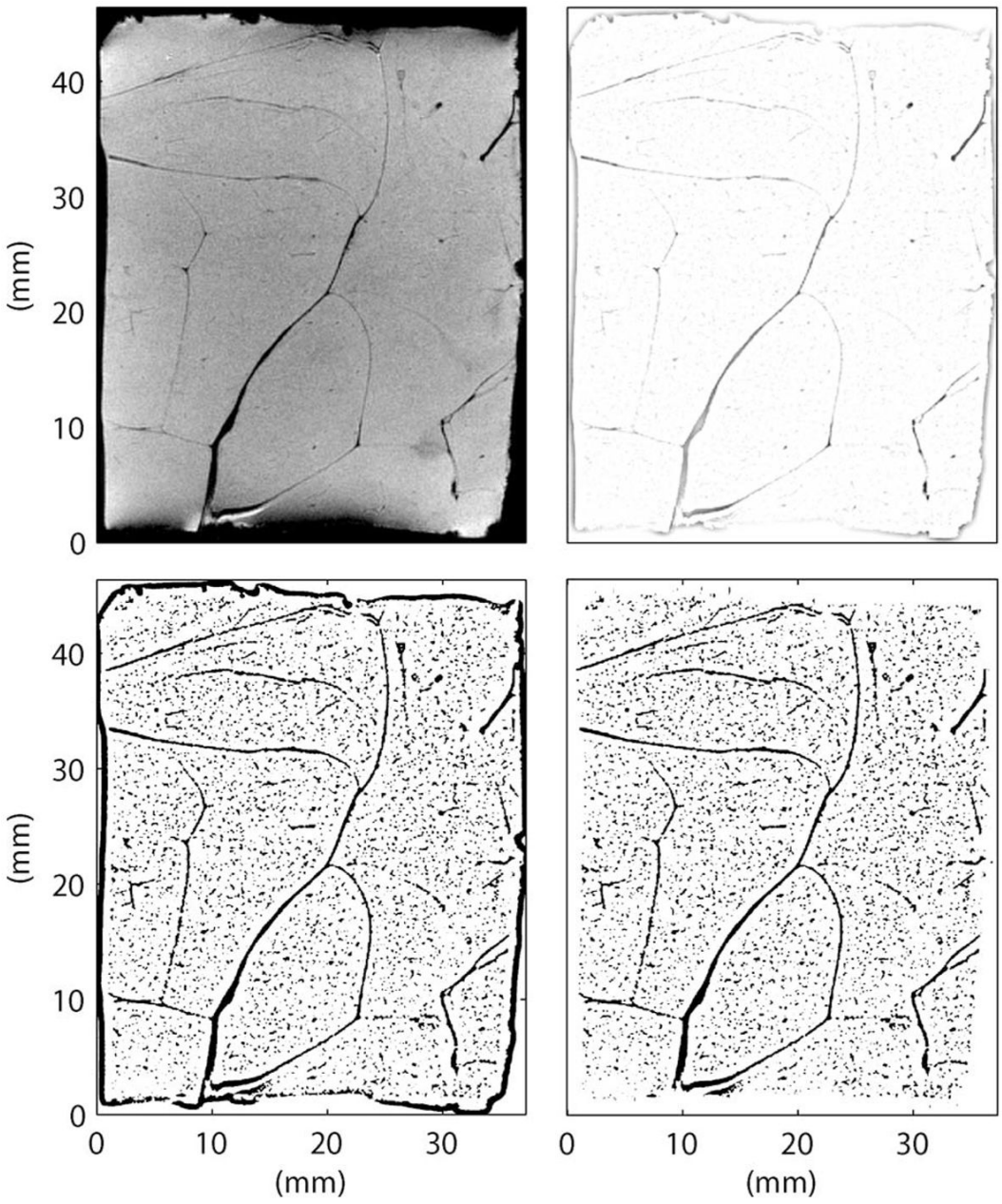

Fig. 5.

Segmentation of fine detail. The top-left panel shows an original cross section after application of a 5 × 5 multilevel bidirectional median filter. The top-right panel shows the difference between the original and filtered cross sections. The bottom-left panel shows the difference after segmentation using a threshold value of 9 on a scale of 0–255. The panel on the bottom right shows the segmented cross section on the left after elimination of the specimen edges.

NIH-PA Author Manuscript
NIH-PA Author Manuscript
NIH-PA Author Manuscript

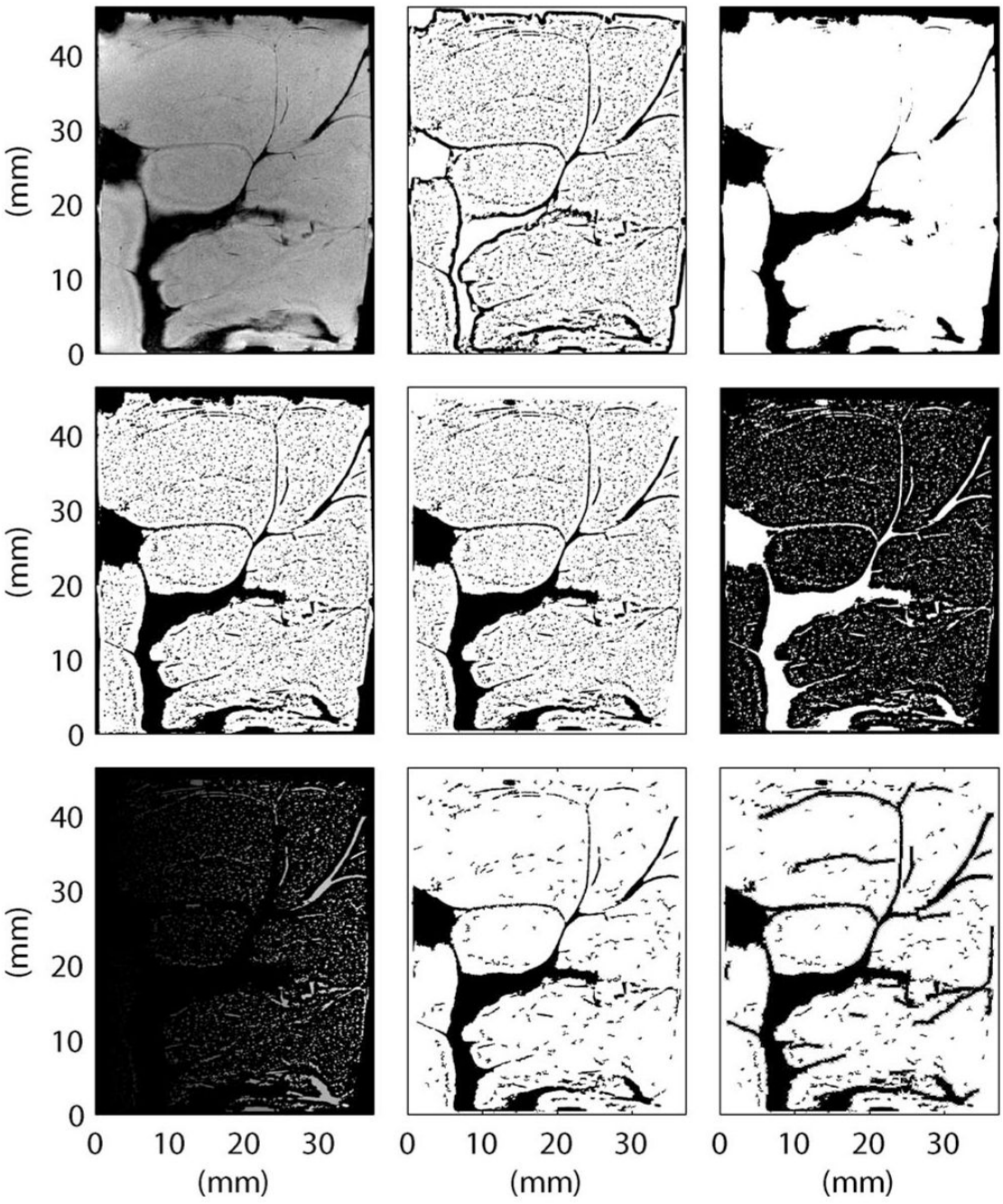

Fig. 6.

Segmentation based on a procedure that preserves fine detail and large features. The top row shows, from left to right, a nonlinearly filtered image, an image segmented for fine detail, and an image segmented using the Otsu thresholding. The center row shows, from left to right, the result of using a combination of thresholding for fine detail and the Otsu thresholding for large features, the result of eliminating the specimen edges, and a contrast-inverted image, also without specimen edges. The bottom row shows, from left to right, a labeled contrast-inverted image, an image after eliminating small objects and stray voxels, and an image after the application of a morphologic filter.

NIH-PA Author Manuscript
NIH-PA Author Manuscript
NIH-PA Author Manuscript

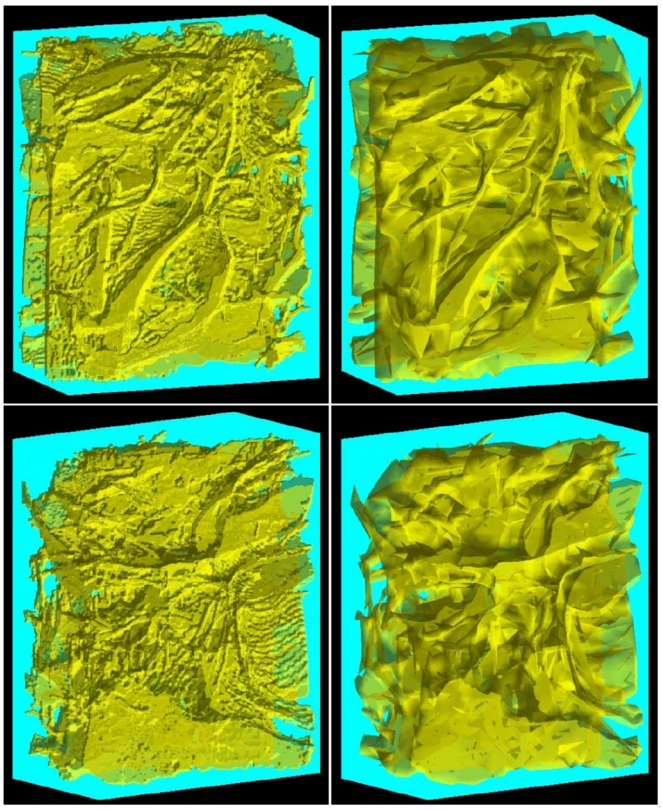

Fig. 7.

Aliasing and aliasing suppression. Visualizations in the left column show isosurfaces with aliasing artifacts. Visualizations in the right column show the result of using a 3-D Gaussian smoothing filter to suppress aliasing. The structures represent connective tissue, while the transparent background represents fat. The top row of panels shows a different perspective than the bottom row of panels.

NIH-PA Author Manuscript

NIH-PA Author Manuscript

NIH-PA Author Manuscript

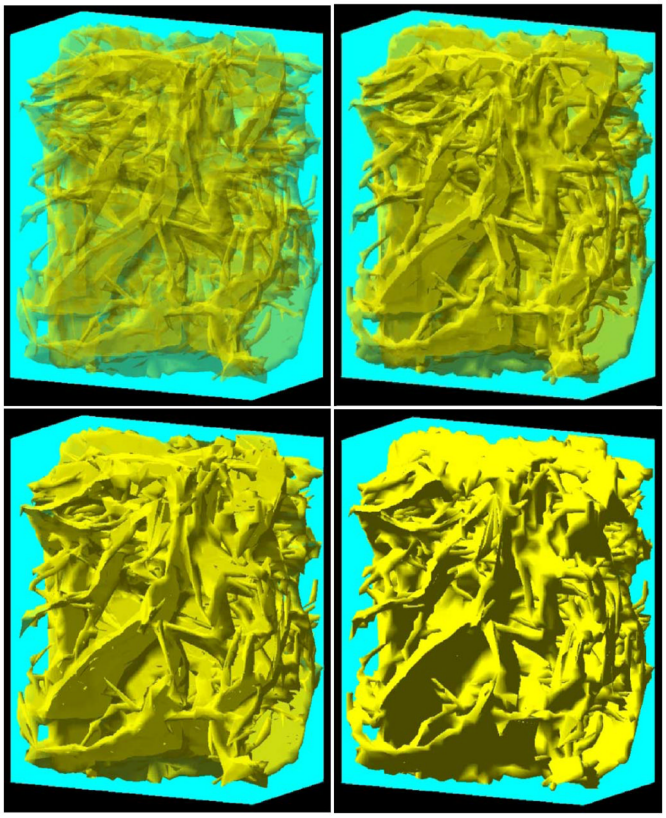

Fig. 8.

The effect of transparency on visualization. Isosurfaces having transparency values of 0.3, 0.5, 0.75, and 1.0, respectively, are shown with transparency increasing from left to right and top to bottom. Transparencies about midway in the range from 0 (totally transparent) to 1 (totally opaque) render the morphology most understandably.

NIH-PA Author Manuscript
NIH-PA Author Manuscript
NIH-PA Author Manuscript

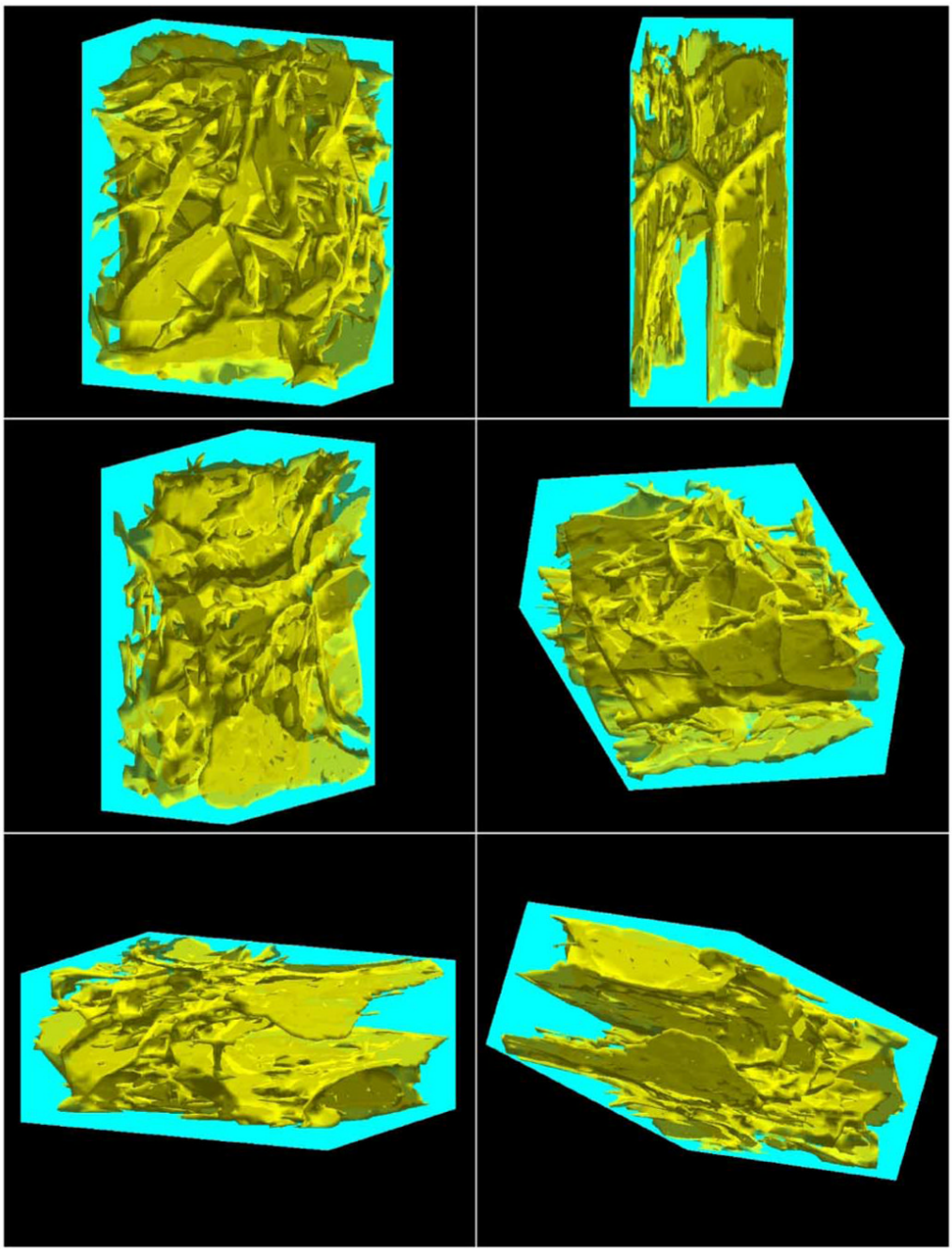

Fig. 9.
Morphology of the breast tissue specimen. The tissue volume is shown from different viewing angles to enhance appreciation of the structure. The visualization uses isosurfaces with a transparency value of 0.6 and Phong parameters of 0.3, 0.8, and 0 for ambient, diffuse, and specular light, respectively.

NIH-PA Author Manuscript

NIH-PA Author Manuscript

NIH-PA Author Manuscript

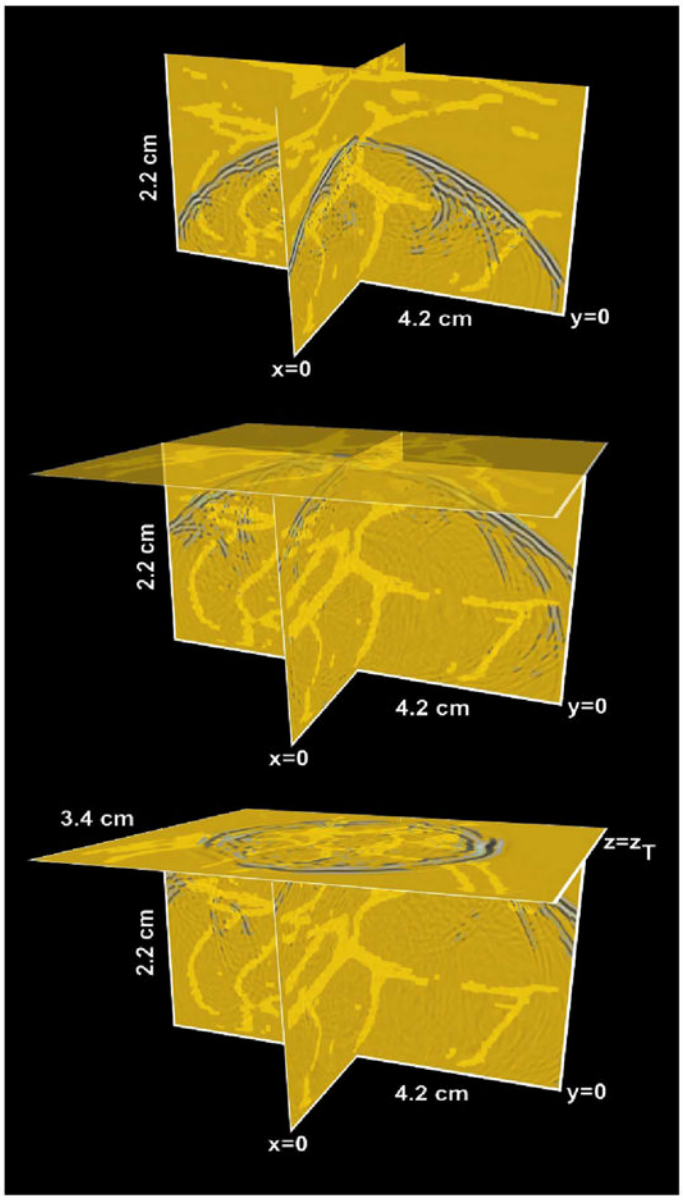

Fig. 10.

Representative instants during propagation of an ultrasound pulse wave through a segmented specimen of breast. Distortion, scattering, and diffraction are caused by the inhomogeneous structure of the breast as the wave advances through the model from the instant in the top panel to the instant in the bottom panel.

NIH-PA Author Manuscript

NIH-PA Author Manuscript

NIH-PA Author Manuscript

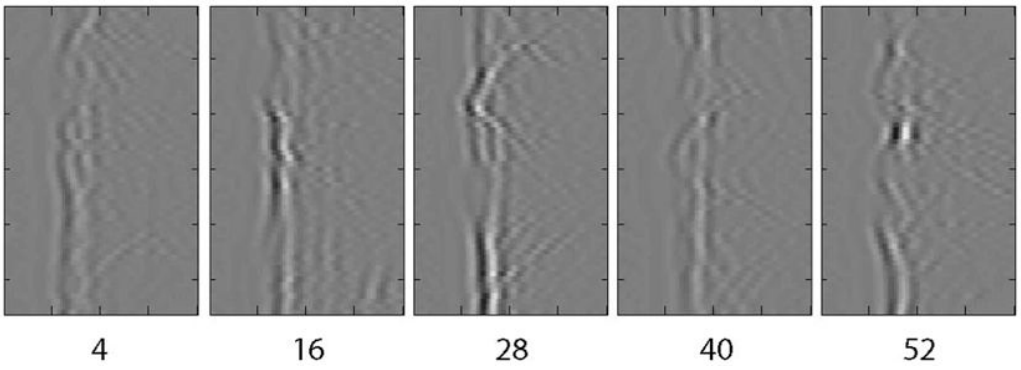

Fig. 11.

Aperture Waveforms. The waveforms, corrected for geometry associated with the apparent source location, received in representative rows of the simulated 57 × 57 aperture are shown on a linear scale. The row number is below the horizontal axis that spans a time of 4 μs (80 samples). The vertical axis spans 34.2 mm.

NIH-PA Author Manuscript

NIH-PA Author Manuscript

NIH-PA Author Manuscript

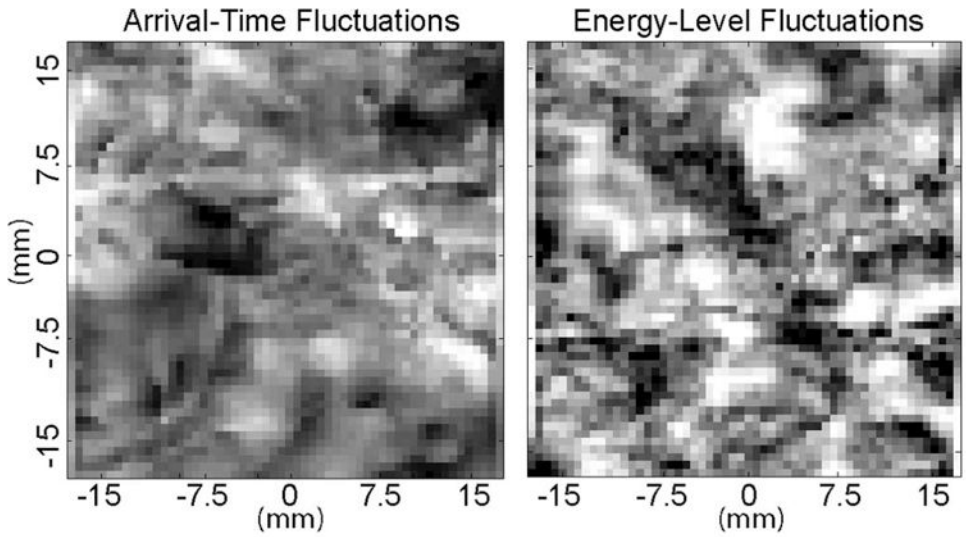

Fig. 12.

Arrival-time fluctuations and energy-level fluctuations. The fluctuations resulted from numerical propagation of an ultrasonic pulse through an acoustic model based on the segmented specimen of human breast. The arrival-time fluctuations, shown using a linear gray scale with a dynamic range of ±150 ns, have an rms value of 58.6 ns. The energy-level fluctuations, shown using a gray scale with a dynamic range of ±11 dB, have an rms value of 3.2 dB.

NIH-PA Author Manuscript
NIH-PA Author Manuscript
NIH-PA Author Manuscript

Table I

Comparison of Statistics Computed From Measurements [4] of Propagation and Propagation Through a Model

	Thickness (mm)	Arrival-Time RMS Value (ns)	Fluctuations Corr. Len. (mm)	Energy-Level RMS Value (dB)	Fluctuations Corr. Len. (mm)
Measured Data	22	61	4.1	4.7	2.8
Model Data	22	59	4.0	3.2	2.4

The row labeled “Measured Data” is the average from measurements of comparable specimens of human breast. The row labeled “Model Data” are the corresponding statistics from calculated propagation through the breast model. The correlation lengths are the full-width at half-maximum spatial-correlation lengths for the two sets of fluctuations.